

ATMOSPHERIC SCIENCE

Isotopic evidence for acidity-driven enhancement of sulfate formation after SO₂ emission control

Shohei Hattori^{1*}, Yoshinori Iizuka², Becky Alexander³, Sakiko Ishino^{1,4}, Koji Fujita⁵, Shuting Zhai³, Tomás Sherwen^{6,7}, Naga Oshima⁸, Ryu Uemura⁵, Akinori Yamada⁹, Nozomi Suzuki¹, Sumito Matoba², Asuka Tsuruta¹, Joel Savarino¹⁰, Naohiro Yoshida^{1,11,12}

After the 1980s, atmospheric sulfate reduction is slower than the dramatic reductions in sulfur dioxide (SO₂) emissions. However, a lack of observational evidence has hindered the identification of causal feedback mechanisms. Here, we report an increase in the oxygen isotopic composition of sulfate ($\Delta^{17}\text{O}_{\text{SO}_4^{2-}}$) in a Greenland ice core, implying an enhanced role of acidity-dependent in-cloud oxidation by ozone (up to 17 to 27%) in sulfate production since the 1960s. A global chemical transport model reproduces the magnitude of the increase in observed $\Delta^{17}\text{O}_{\text{SO}_4^{2-}}$ with a 10 to 15% enhancement in the conversion efficiency from SO₂ to sulfate in Eastern North America and Western Europe. With an expected continued decrease in atmospheric acidity, this feedback will continue in the future and partially hinder air quality improvements.

INTRODUCTION

Atmospheric sulfate (SO₄²⁻) has a notable but uncertain impact on the global radiation budget and cloud lifetimes (1). Sulfate also accounts for a major component of fine particulate matter mass in urban regions, affecting visibility (2) and public health (3). Since the Industrial Revolution, increased emissions of sulfur dioxide (SO₂) have resulted in an increase in sulfate load. The period from the 1950s to the 1970s had increased SO₂ emissions leading to high-pollution; however, switching to cleaner technology and fuels decreased these emissions after the 1980s across North America (NA) and Western Europe (WE) (4). These decreases successfully lowered sulfate concentrations, which avoided hundreds of thousands of deaths and illnesses from exposure to particulate matter smaller than 2.5 μm (PM_{2.5}) in the United States alone (3). However, atmospheric sulfate declined less rapidly than SO₂ emissions, especially in wintertime (4–6). This unexpected phenomenon suggests the existence of feedback processes, which render SO₂ emission reductions less efficient than expected for mitigation of sulfate aerosol.

In the atmosphere, the majority (60 to 80%) of sulfate formation occurs through oxidation of SO₂ in the aqueous phase (i.e., in clouds), with gas-phase SO₂ oxidation by hydroxyl radicals (•OH) accounting for most of the remainder (20 to 40%) (7). Upon dissolution in the aqueous phase, SO₂ dissociates into S(IV) species (mainly HSO₃⁻ and SO₃²⁻) that react with hydrogen peroxide (H₂O₂), ozone (O₃), molecular oxygen (O₂), and hypohalous acid (e.g., HOBr) to form sulfate (8). S(IV) oxidation is thought to be dominated by H₂O₂ oxidation, which is largely insensitive to cloud

acidity, whereas the more minor S(IV) + O₃ pathway exhibits strong pH dependence (8). Among these chemical processes, several studies have proposed enhancement of S(IV) + H₂O₂ (9, 10), S(IV) + O₃ (11), or SO₂ + •OH (10, 12) oxidation pathways as mechanisms causing the weakened response of sulfate abundances to decreases in SO₂ emissions. These conclusions are based on a comparison between observed and modeled sulfate concentrations, and model estimates of atmospheric sulfate production mechanisms. However, observational evidence so far has not pointed to a specific mechanism. These uncertainties limit confidence in the model forecast and hindcasts of management of current and future tropospheric sulfate aerosol and its environmental impacts.

One tool for providing insight into sulfate formation mechanisms is offered by the mass-independent oxygen isotopic composition ($\Delta^{17}\text{O}$) (13) of sulfate (see Materials and Methods). $\Delta^{17}\text{O}_{\text{SO}_2}$ equals 0‰ because of rapid oxygen exchange between SO₂ and H₂O in the atmosphere (14), and thus the $\Delta^{17}\text{O}_{\text{SO}_4^{2-}}$ value reflects the oxidation pathway of SO₂ to SO₄²⁻. Gas-phase SO₂ oxidation by •OH, where $\Delta^{17}\text{O}_{\text{•OH}} = 0\text{‰}$, produces SO₄²⁻ with $\Delta^{17}\text{O}_{\text{SO}_4^{2-}} = 0\text{‰}$ (15). Aqueous-phase S(IV) oxidation by H₂O₂ and O₃ leads to nonzero $\Delta^{17}\text{O}_{\text{SO}_4^{2-}}$ values through transfer of the nonzero $\Delta^{17}\text{O}$ from the oxidants. $\Delta^{17}\text{O}_{\text{H}_2\text{O}_2}$ has been reported to be $1.6 \pm 0.3\text{‰}$ (16), and the transfer factor from oxidant to sulfate is 0.5 based on a laboratory experiment (15), which yields $\Delta^{17}\text{O}_{\text{SO}_4^{2-}}$ values for S(IV) oxidation by H₂O₂ [$\Delta^{17}\text{O}_{\text{SO}_4^{2-}(\text{H}_2\text{O}_2)}$] of $0.8 \pm 0.2\text{‰}$. For $\Delta^{17}\text{O}_{\text{O}_3}$, the two earliest studies using a cryogenic technique showed a large range over $\pm 10\text{‰}$ (17, 18). This range is much greater than expected from the pressure and temperature dependency of $\Delta^{17}\text{O}_{\text{O}_3}$ (19–21). On the basis of these experimental data, the large variability found in the two early studies using cryogenic techniques would be caused by random errors associated with sampling artifacts (22). We therefore exclude these two studies from consideration and instead use the average value of the tropospheric $\Delta^{17}\text{O}_{\text{O}_3}$ with $25.6 \pm 1.3\text{‰}$ originating from the observations using nitrite-coated method among different locations and seasons (23–25). As a consequence, the $\Delta^{17}\text{O}_{\text{SO}_4^{2-}}$ values for S(IV) + O₃ [$\Delta^{17}\text{O}_{\text{SO}_4^{2-}(\text{O}_3)}$] is assumed to be $6.4 \pm 0.3\text{‰}$, using a transferring factor of 0.25 based on a laboratory study (15). The S(IV) + O₂ reaction catalyzed by trace metal ions (TMI) produces $\Delta^{17}\text{O}_{\text{SO}_4^{2-}(\text{TMI})}$ of -0.1‰ by transferring one oxygen atom transferred

¹Department of Chemical Science and Engineering, School of Materials and Chemical Technology, Tokyo Institute of Technology, Yokohama 226-8502, Japan. ²Institute of Low Temperature Science, Hokkaido University, Sapporo 060-0819, Japan. ³Department of Atmospheric Sciences, University of Washington, Seattle, WA 98195-1640, USA. ⁴National Institute of Polar Research, Research Organization of Information and Systems, Tokyo 190-8518, Japan. ⁵Graduate School of Environmental Studies, Nagoya University, Nagoya 464-8601, Japan. ⁶National Centre for Atmospheric Science, University of York, York YO10 5DD, UK. ⁷Wolfson Atmospheric Chemistry Laboratories, University of York, York YO10 5DD, UK. ⁸Meteorological Research Institute, Tsukuba 305-0052, Japan. ⁹Toshiba Electric Ltd., Tokyo 170-0005, Japan. ¹⁰University of Grenoble Alpes, CNRS, IRD, Grenoble INP, IGE, F-38000, Grenoble, France. ¹¹Earth-Life Science Institute, Tokyo Institute of Technology, Tokyo 152-8551, Japan. ¹²National Institute of Information and Communications Technology, Tokyo 184-8795, Japan.

*Corresponding author. Email: hattori.s.ab@m.titech.ac.jp or shohato@gmail.com

from atmospheric O_2 [$\Delta^{17}O \approx -0.3\text{‰}$ (26)]. In-cloud HOBr leads to $\Delta^{17}O_{SO_4^{2-}}$ of 0‰, and primary SO_4^{2-} from natural and anthropogenic sources also has $\Delta^{17}O_{SO_4^{2-}} = 0\text{‰}$ (27).

Consequently, $\Delta^{17}O_{SO_4^{2-}}$ is solely determined by the proportions of different sulfate formation pathways that yield nonzero values of $\Delta^{17}O_{SO_4^{2-}}$ (28)

$$\Delta^{17}O_{SO_4^{2-}} = \Delta^{17}O_{SO_4^{2-}(O_3)}f_{O_3} + \Delta^{17}O_{SO_4^{2-}(H_2O_2)}f_{H_2O_2} + \Delta^{17}O_{SO_4^{2-}(TMI)}f_{TMI} + 0f_{zero} \quad (1)$$

where the f_x ($x = O_3, H_2O_2, TMI,$ and zero) terms indicate the respective fractions of SO_2 oxidized by O_3, H_2O_2, TMI -catalyzed O_2 , and oxidants which have $\Delta^{17}O_{SO_4^{2-}} = 0\text{‰}$, and $f_{O_3} + f_{H_2O_2} + f_{TMI} + f_{zero} = 1$ (see Supplementary Text). To date, this approach using $\Delta^{17}O_{SO_4^{2-}}$ has enabled observation-based quantification of atmospheric sulfate formation in different regions and time periods, including glacial-interglacial cycles (29), stratospheric volcanic eruptions (30), preindustrial biomass burning (31), and transition after the Industrial Revolution (32). In particular, comparison of observed and modeled $\Delta^{17}O_{SO_4^{2-}}$ has enabled the recognition and quantification of sulfate formation mechanisms often ignored in models, including $S(IV) + O_2$ oxidation catalyzed by TMI (32, 33), sulfate formation by ozone oxidation on sea salt aerosol (34), $S(IV)$ oxidation by hypohalous acids (35, 36), and heterogeneous reactions in extreme haze events (28, 37). However, there is no record of $\Delta^{17}O_{SO_4^{2-}}$ that can provide information on changes in sulfate formation pathways in response to the reduction in air pollution following the implementation of governmental reduction policy such as the U.S. Clean Air Act of 1970.

Here, we present the first observations of changes in Northern Hemisphere $\Delta^{17}O_{SO_4^{2-}}$ between 1959 and 2015, based on a continuous and high-resolution ice core record from a high-elevation dome site in southeast Greenland called SE-Dome. The record from the past 60 years covers the high-pollution decades of the 1950s to 1970s as well as the substantial SO_2 emissions-reduction period from the 1980s to the present (1). The SE-Dome ice core preserves atmospheric aerosols that originate mainly from NA and WE, with no notable change in the air mass origin over the period (38). We reconstructed $\Delta^{17}O_{SO_4^{2-}}$ in 3 to 6 years resolution with an accuracy of dating better than 2 months, which is given by precise age-depth scaling with the oxygen-isotope matching method (39).

RESULTS

Increase of ice core $\Delta^{17}O_{nss-SO_4^{2-}}$ over the past 60 years

The ice core $\Delta^{17}O_{nss-SO_4^{2-}}$ ranges from 1.0‰ to 1.7‰ and shows a substantial increase throughout the record (Fig. 1A), with a $\sim 0.4\text{‰}$ difference ($P < 0.05$) between the $\Delta^{17}O_{nss-SO_4^{2-}}$ average of 1960 to 1970 ($1.14 \pm 0.05\text{‰}$, $n = 4$) and that of 2005 to 2015 ($1.51 \pm 0.19\text{‰}$, $n = 3$). This increase in $\Delta^{17}O_{nss-SO_4^{2-}}$ clearly indicates that the sulfate formation pathways responsible for sulfate preserved in the SE-Dome have changed from the 1960s to the present. Given that the $\Delta^{17}O_{SO_4^{2-}}$ signatures for the sulfate formation pathways are all lower than 0.8‰ except for the $S(IV) + O_3$ pathway [$\Delta^{17}O_{SO_4^{2-}(O_3)} = 6.4 \pm 0.3\text{‰}$], the $\Delta^{17}O_{nss-SO_4^{2-}}$ increase can reasonably be interpreted as the reflection of an increase in the relative importance of the $S(IV) + O_3$ pathway.

By applying a simple isotope mass balance method (Eqs. 2 and 3), we calculated the maximum and minimum contribution of oxidation by the $S(IV) + O_3$ pathway ($f_{O_3, \max}$ and $f_{O_3, \min}$)

$$f_{O_3, \max} = (\Delta^{17}O_{nss-SO_4^{2-}} - \Delta^{17}O_{SO_4^{2-}(TMI)}) / (\Delta^{17}O_{SO_4^{2-}(O_3)} - \Delta^{17}O_{SO_4^{2-}(TMI)}) \quad (2)$$

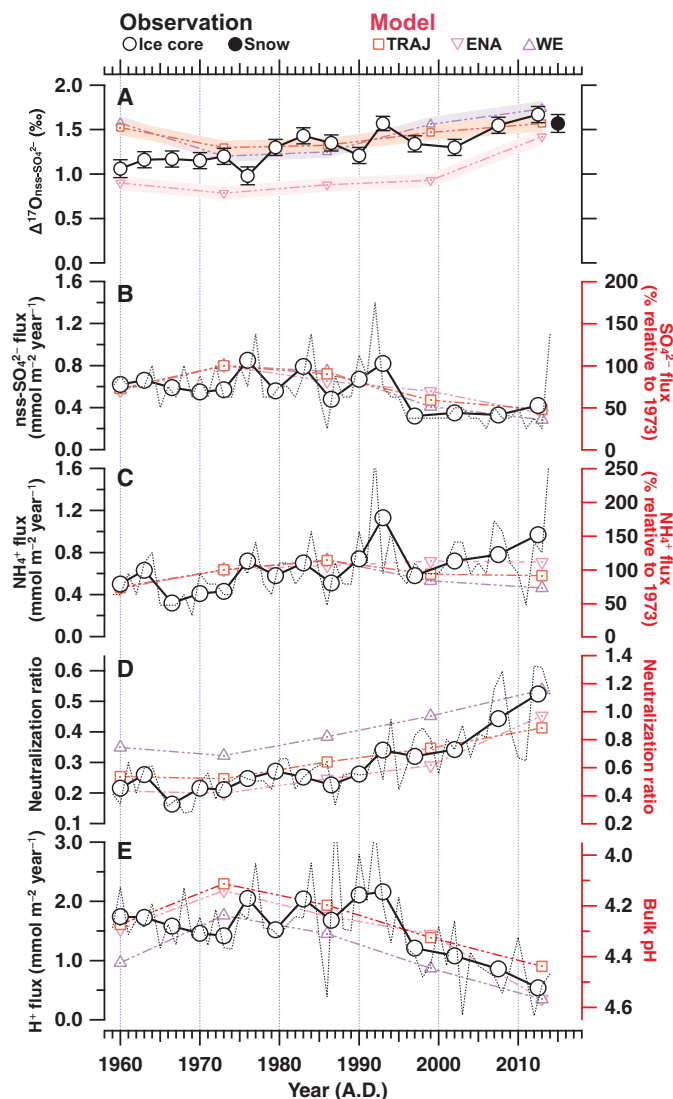


Fig. 1. $\Delta^{17}O_{nss-SO_4^{2-}}$ and chemical fluxes at the SE-Dome and GEOS-Chem model results during the last 60 years. Open black circles represent ice core record, the closed black circle represents data for shallow snow pit, and colored symbols represent model results for given years for TRAJ, ENA, and WE regions. The observed chemical fluxes and neutralization ratio were obtained from Iizuka *et al.* (38). The thin lines represent observed data for each year, and the open circles with thick lines represent the weighted average flux data corresponding to $\Delta^{17}O_{SO_4^{2-}}$ sample resolution (see Supplementary Text). (A) $\Delta^{17}O_{SO_4^{2-}}$ record. Open black circles represent ice core record and the closed black circle represents data for shallow snow with 1σ uncertainty shown as error bar. Colored symbols represent annual-mean, mass-weighted average of tropospheric $\Delta^{17}O_{SO_4^{2-}}$ for given years. The shaded area for the modeled $\Delta^{17}O_{SO_4^{2-}}$ indicates the 1σ uncertainty. (B) $nss-SO_4^{2-}$ flux and modeled annual-mean SO_4^{2-} concentration normalized to 1973 (C) NH_4^+ flux and modeled annual-mean concentrations of $NH_3 + NH_4^+$ normalized to 1973, (D) neutralization ratio: $NH_4^+ / (2 nss-SO_4^{2-} + NO_3^-)$ for observation, and $(NH_4^+ + NH_3) / [2 nss-SO_4^{2-} + (NO_3^- + HNO_3)]$ calculated from modeled, annual-mean tropospheric concentrations, and (E) H^+ flux and modeled tropospheric annual-mean, cloud liquid water weighted, bulk cloud pH.

$$f_{O_3, \min} = (\Delta^{17}O_{\text{nss-SO}_4^{2-}} - \Delta^{17}O_{\text{SO}_4^{2-}(\text{H}_2\text{O}_2)}) / (\Delta^{17}O_{\text{SO}_4^{2-}(\text{O}_3)} - \Delta^{17}O_{\text{SO}_4^{2-}(\text{H}_2\text{O}_2)}) \quad (3)$$

The $f_{O_3, \max}$ is estimated from the two end-members mixing between the S(IV) + O₃ reaction and the S(IV) + O₂ reaction catalyzed by TMI, which has the lowest end-member of $\Delta^{17}O_{\text{nss-SO}_4^{2-}}$ (i.e., -0.1‰). The $f_{O_3, \min}$, on the other hand, is calculated based on the mixing between the S(IV) + O₃ pathway and the S(IV) + H₂O₂ pathway. Using these equations, the lowest $f_{O_3, \min}$ and $f_{O_3, \max}$ values were, respectively, calculated to be $3.2 \pm 0.9\%$ and $16.6 \pm 1.9\%$ for years 1975 to 1977 ($\Delta^{17}O_{\text{nss-SO}_4^{2-}} = 0.98 \pm 0.10\text{‰}$; sample 6 in table S1). These $f_{O_3, \min}$ and $f_{O_3, \max}$ values, respectively, increase to $15.5 \pm 4.2\%$ and $27.2 \pm 1.9\%$ at maximum $\Delta^{17}O_{\text{nss-SO}_4^{2-}}$ of $1.67 \pm 0.09\text{‰}$ (years 2011 to 2014, sample 15 in table S1). The increase of the relative importance of the S(IV) + O₃ pathway can be explained by (i) enhancement of the S(IV) + O₃ pathway itself and (ii) decrease of other oxidation pathways that have lower $\Delta^{17}O_{\text{SO}_4^{2-}}$ values.

First, we consider the possible reasons that could cause an enhancement of the S(IV) + O₃ pathway. Given that high pH conditions promote the S(IV) + O₃ pathway (8), acidity changes may be an important factor accounting for the increase in $\Delta^{17}O_{\text{nss-SO}_4^{2-}}$. The best correlation between $\Delta^{17}O_{\text{nss-SO}_4^{2-}}$ and other ice core measurements is found for the neutralization ratio, $\text{NH}_4^+ / (2 \text{nss-SO}_4^{2-} + \text{NO}_3^-)$ (Fig. 1D), where $r = 0.80$ ($P < 0.01$; table S1). In addition, the H⁺ flux (Fig. 1E), the ice acidity indicator, also shows a strong correlation with $\Delta^{17}O_{\text{nss-SO}_4^{2-}}$ ($r = -0.71$, $P < 0.01$; table S1). The increase in the neutralization ratio and the decrease in the acidity result from the simultaneous decrease in nss-SO₄²⁻ flux (Fig. 1B) and increase in NH₄⁺ flux (Fig. 1C). This is consistent with previous studies that observed an increase in the pH of precipitation in NA and WE after the 1970s (40) and in a Greenland ice core (41), mainly because of the mitigation of SO₂ emission and the simultaneous increase in NH₃ emission from agricultural and industrial sectors (42). Changes in O₃ concentrations over the period may also contribute to changes in sulfate formation pathways. Tropospheric O₃ concentrations in the free troposphere [~ 3 km above sea level (a.s.l.)] increased by 1 to 3 ppbv (parts per billion by volume) decade⁻¹ from the 1970s to 2000s, but there is no significant subsequent increase (43). Thus, an increase in tropospheric O₃ might partially contribute to the increase of the S(IV) + O₃ pathway before 2000 but is not consistent with the substantial increase of $\Delta^{17}O_{\text{nss-SO}_4^{2-}}$ for the post-year 2000 period (Fig. 1A).

Second, we discuss the possibility of inhibition of other oxidation pathways that have low $\Delta^{17}O_{\text{nss-SO}_4^{2-}}$, because the decrease of other sulfate formation pathways could also increase the relative importance of the S(IV) + O₃ pathway. Influence from changes in the contribution from SO₂ + OH due to changes in tropospheric •OH concentrations is thought to be minimal, given that no significant decrease in •OH is observed between 1980 and 2010 (44). Greenland ice core shows a post-1950 increase of H₂O₂ (45), but this H₂O₂ increase is not consistent with the observed $\Delta^{17}O_{\text{nss-SO}_4^{2-}}$ increase, given the $\Delta^{17}O_{\text{SO}_4^{2-}}$ values of only 0.8‰ from S(IV) + H₂O₂ reaction. An observed 0.6‰ decrease in $\Delta^{17}O_{\text{nss-SO}_4^{2-}}$ in a Greenland ice core from 1900 to 1980 was partially attributed to an increase in the TMI-catalyzed S(IV) + O₂ oxidation pathway resulting from increases in anthropogenic metal emission after the Industrial Revolution (32). A decrease in anthropogenic metal emissions since 1980 would tend to decrease the importance of the TMI-catalyzed S(IV) +

O₂ oxidation pathway, resulting in an increase in $\Delta^{17}O_{\text{nss-SO}_4^{2-}}$ as observed.

The GEOS-Chem model reproduces the observed increase of $\Delta^{17}O_{\text{nss-SO}_4^{2-}}$

To examine the relative importance changes in sulfate formation mechanisms on observed ice core $\Delta^{17}O_{\text{nss-SO}_4^{2-}}$, we simulate global tropospheric chemistry using the GEOS-Chem chemical transport model (version 12.5.0, DOI: 10.5281/zenodo.3403111) with an updated “offline” tagged-sulfate aerosol simulation (32, 33, 46). We performed model simulations using meteorology and anthropogenic emissions for the years 1960, 1973, 1986, 1999, and 2013 (see Materials and Methods). This model calculates bulk cloud pH based on the local concentrations of inorganic species and CO₂ (g) and considers the impact of heterogeneity in cloud water pH within a cloud (35). Because the main source region of sulfate aerosol to the Arctic region is transported from Eastern North America (ENA) and WE, we compare the ice core observations with modeled tropospheric $\Delta^{17}O_{\text{SO}_4^{2-}}$ in ENA (-90° to -60°E, 30° to 60°N, $n = 56$) and WE (15° to 40°E, 40° to 70°N, $n = 72$) (fig. S2). We also compute modeled $\Delta^{17}O_{\text{SO}_4^{2-}}$ in the region -90° to 30°E and 35° to 90°N based on computed 10-day back trajectories [$n = 300$, Trajectory (TRAJ) region hereafter] (fig. S2) (38).

In Fig. 1A, the modeled, annual-mean, mass-weighted average of tropospheric $\Delta^{17}O_{\text{SO}_4^{2-}}$ for five periods is shown. The model calculates a decrease of $\Delta^{17}O_{\text{SO}_4^{2-}}$ from 1960 to 1973 and an increase of $\Delta^{17}O_{\text{SO}_4^{2-}}$ from 1973 to 2013 for all three regions for TRAJ, ENA, and WE. Note that the SO₂ emission is still increasing from 1960 to 1975 (Fig. 1B), and the $\Delta^{17}O_{\text{SO}_4^{2-}}$ in the model shows a decrease (Fig. 1A). This decrease in $\Delta^{17}O_{\text{SO}_4^{2-}}$ is not clearly observed in the ice core $\Delta^{17}O_{\text{nss-SO}_4^{2-}}$ record, but one data point covering the year 1975 (sample 6, table S1) shows the lowest $\Delta^{17}O_{\text{SO}_4^{2-}}$ with $0.98 \pm 0.10\text{‰}$ within the study period (Fig. 1A). Overall, the observed $\Delta^{17}O_{\text{SO}_4^{2-}}$ falls within modeled values in all years, consistent with a mixture of sulfate originating in ENA and WE. The increase in modeled $\Delta^{17}O_{\text{SO}_4^{2-}}$ is due to an increase in f_{O_3} between 1973 and 2013 from 8.0 to 18.0% for the ENA region and 16.3 to 23.7% for the WE region, respectively (fig. S3), consistent with the observation-based estimate of an increase in f_{O_3} from 3.2 to 16.6% (1960 to 1970s) to 15.5 to 27.2% (present).

GEOS-Chem reproduces not only the observed $\Delta^{17}O_{\text{nss-SO}_4^{2-}}$ trend, but also other trends for modeled sulfate (Fig. 1B), NH₄⁺ (Fig. 1C), neutralization ratio (Fig. 1D), and bulk cloud pH (Fig. 1E) between 1973 and 2013. Modeled bulk cloud pH increased by 0.5 pH units between 1973 and 2013 (Fig. 1E) and neutralization ratio also shows substantial increases between 1973 and 2013 (Fig. 1D), with good agreement with modeled changes in $\Delta^{17}O_{\text{SO}_4^{2-}}$ for ENA and WE ($r > 0.75$, $P < 0.01$; table S2). In addition, no increase in the modeled $\Delta^{17}O_{\text{SO}_4^{2-}}$ is found when cloud pH is set constant to pH 4.5 in the model (fig. S6). The TMI-catalyzed S(IV) + O₂ pathway, on the other hand, decreases by $\sim 10\%$ in the model between 1973 and 2013, yielding a 0.1‰ increase in $\Delta^{17}O_{\text{SO}_4^{2-}}$ (fig. S3). Although this goes in the right direction, it is not large enough to explain the observed 0.7‰ increase in $\Delta^{17}O_{\text{SO}_4^{2-}}$. Modeled O₃ concentrations also increase over this same time period, but the increase from 1960 to 1986 is higher than from 1986 to 2013 (fig. S4) and correlation between O₃ concentrations to the modeled $\Delta^{17}O_{\text{SO}_4^{2-}}$ is not significant (table S2). Overall, we conclude that the modeled increase in $\Delta^{17}O_{\text{nss-SO}_4^{2-}}$ is mainly driven by an increase in the cloud water pH over the same time period.

DISCUSSION

Enhancement of sulfate formation efficiency

We use the model to further investigate how changes in sulfate formation pathways alter the conversion efficiency (η) from SO_2 to SO_4^{2-} using the following metric

$$\eta_x = P(\text{SO}_4^{2-})_x / S(\text{SO}_2) \quad (4)$$

where $P(\text{SO}_4^{2-})_x$ indicates the tropospheric sulfate production rate from the oxidation of SO_2 by oxidant x [i.e., OH , H_2O_2 , O_3 , O_2 (TMI), and hypohalous acids (H)], and $S(\text{SO}_2)$ represents total tropospheric source SO_2 calculated from SO_2 emission, photochemical SO_2 production, and net transport (import – export). Although there is regional variability (fig. S7), the common feature in all regions is that η decreases until 1973 and increases from 1973 to 2013. The decreases in total η from 1960 to 1973 are caused mainly by decreases in η_{O_3} and $\eta_{\text{H}_2\text{O}_2}$ for ENA, and caused by decreases in η_{O_3} but compensated by increases in η_{OH} for WE, respectively (Fig. 2, A and B). By contrast, the 10 to 15% increases in total η from 1973 to 2013 found in ENA and WE are caused mainly by increases in η_{O_3} and $\eta_{\text{H}_2\text{O}_2}$ particularly in ENA, but are partially compensated by decreases in η_{TMI} and η_{OH} (Fig. 2, A and B). The modeled increase of η in ENA after 1999 wintertime (fig. S8B) is consistent with a weakened response of reduction of U.S. SO_2 emission due to combination of a weakening H_2O_2 limitation on the $\text{S(IV)} + \text{H}_2\text{O}_2$ pathway (9) and cloud pH-induced promotion of $\text{S(IV)} + \text{O}_3$ pathway at low SO_2 (11).

It is worth noting that there is a regional difference of changes in η and corresponding processes between ENA and WE after SO_2 emission control. In contrast to ENA, the WE region has relatively high coal combustion and thus higher metal emissions, yielding a higher contribution from the TMI-catalyzed $\text{S(IV)} + \text{O}_2$ oxidation in wintertime (fig. S8C). Increases of η_{O_3} and $\eta_{\text{H}_2\text{O}_2}$ for WE between 1973 and 2013 are 10 and 8%, respectively, but these increases were compensated by a decrease of η_{TMI} by 5% (Fig. 2B). Notably, the main contribution for total η for WE was switched from the TMI-catalyzed $\text{S(IV)} + \text{O}_2$ oxidation in 1973 to the $\text{S(IV)} + \text{O}_3$ oxidation in 2013 (Fig. 2B). An increase in η_{O_3} in WE thus plays a greater role for the increase of η compared to ENA, because of relatively high cloud pH conditions (Fig. 1E) and more limited oxidant concentrations at higher latitude. The relatively small decreases in η_{OH} and increase in η_{H} in both regions are likely driven by an increase in cloud water pH, which enhances SO_2 solubility in clouds (8). As a

consequence, the increase in η over the ENA and WE regions kept sulfate reduction slower than the reduction of source SO_2 during the past 60 years (Fig. 2, A and B) by increasing solubility of SO_2 and promoting the acidity-dependent $\text{S(IV)} + \text{O}_3$ pathway.

The increases in sulfate production efficiency (η) have so far been partially compensated by the reduction of other pathways, particularly in WE (Fig. 2B), but this offset may not be significant in the future. The importance of the $\text{S(IV)} + \text{O}_3$ pathway, on the other hand, will continue to increase in the future because of the increase of cloud water pH by expected future growth of anthropogenic NH_3 emission (47) and possible future usage of NH_3 as hydrogen storage/transport medium in hydrogen energy technologies (48). SO_2 emissions have increased in other parts of the world (e.g., China and India) over the past decades, but they then have been decreasing more recently and are expected to continue to decrease in the coming decades (49, 50). Thus, the acidity-driven enhancement of atmospheric sulfate formation causing nonlinear sulfate responses to SO_2 is expected to occur for the wide area in the world as long as NH_3 emissions are also not simultaneously controlled.

In addition to the SO_4^{2-} burden, changes in sulfate formation pathways have implication for aerosol climatic effects [i.e., size distributions, cloud condensation nuclei (CCN) concentrations and aerosol radiative effect]. In-cloud sulfate production is a potentially important source of accumulation mode-sized CCN due to chemical growth of activated Aitken particles and the enhanced coalescence of processed particles (51). Thus, all-sky aerosol radiative forcing (difference between the 1970–1974 and 2005–2009 periods) over the North Atlantic is modeled to be $+1.2 \text{ W m}^{-2}$ with constant cloud water pH condition at 5.0, but the forcing increases to $+5.2 \text{ W m}^{-2}$ if pH is assumed to increase by 1.0 unit over this period (52). A recent climate model shows that reducing SO_2 emissions at high CO_2 concentrations will significantly enhance atmospheric warming, which is important to consider within the context of the $1.5^\circ\text{C}/2^\circ\text{C}$ target in the Paris Agreement (53). Given that there is regional difference for the chemical feedback process for sulfate formation over the time period in this study (Fig. 2), the future feedback driven by atmospheric acidity for sulfate formation should be predicted locally and globally to design effective mitigation policies for air quality and climate change.

Importance of atmospheric acidity on sulfate formation

In this study, we present ice core $\Delta^{17}\text{O}_{\text{SO}_4^{2-}}$ record providing the first observational evidence that atmospheric acidity has driven

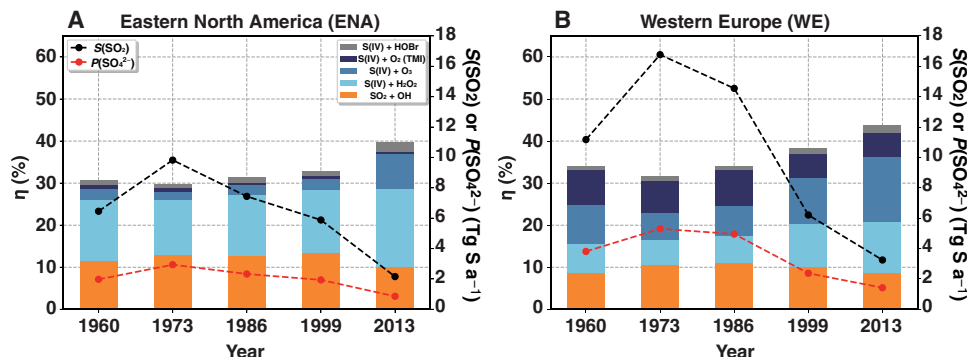


Fig. 2. The conversion efficiency (η) from SO_2 to sulfate (SO_4^{2-}) for each formation pathway (colored bars), annual source SO_2 [$S(\text{SO}_2)$] (black dots), and annual production rate of sulfate [$P(\text{SO}_4^{2-})$] (red dots) calculated in GEOS-Chem. (A) ENA; (B) WE.

changes in sulfate formation pathways as well as enhanced sulfate production rates after SO₂ emissions control in NA and WE. Such identification of key processes for the sulfate formation pathways caused by changes in atmospheric acidity provides confidence in model's forecast for the global sulfur cycle and its relation to climate change, which has not been provided based on only the comparison between observed and modeled sulfate concentrations.

Because atmospheric acidity has a central role for aqueous chemistry in general, cloud/aerosol pH have implications for atmospheric chemistry including not only sulfate but also nitrate, ammonium, halogen, metals, and organic compound reactions that affect air quality, human health, ecosystem, and climate change [(54) and references therein]. However, even for sulfate formation, until the 1990s, cloud pH was considered too low to allow the S(IV) + O₃ reaction to occur, leading modeling studies to often neglect this S(IV) + O₃ oxidation mechanism for sulfate formation (55, 56). Although recent studies have proposed the importance of cloud water pH promoting the S(IV) + O₃ pathway as a possible factor explaining the sublinear response of SO₄²⁻ concentrations to the decrease in SO₂ emission (47, 57), even the latest study (52) prescribes a constant cloud pH in the estimation for radiative forcing effect via aerosols. The relative contribution of the S(IV) + O₃ pathway to total SO₄²⁻ production remains uncertain, ranging from 1 to 50% among model results (11), and suffers from a lack of observational evidence. In this context, the Δ¹⁷O_{SO₄²⁻ values obtained from both atmospheric observation and ice core records provide the validation of changes in sulfate formation pathways and its climatic effects in response to the reduction in air pollution such as the U.S. Clean Air Act of 1970.}

Although the increasing trends in Δ¹⁷O_{SO₄²⁻ were found in both observations and model after SO₂ emission control, several nonnegligible uncertainties for the modeled Δ¹⁷O_{SO₄²⁻ remain (see Supplementary Text). In addition, there are several factors controlling Δ¹⁷O_{SO₄²⁻ in the atmosphere, indicating that it is not possible to use Δ¹⁷O_{SO₄²⁻ as a simple proxy for reconstructing cloud water pH. Similarly, as for the pH assumption in chemical transport models, spatial and temporal variability in clouds, which are challenging to predict and represented differently across models, could contribute to some of this model variability (54). Long-term records of Δ¹⁷O_{SO₄²⁻ are rare and so far limited, but it is possible to reconstruct temporal variations from various ice cores from Arctic and Antarctic ice sheets and from mountain glaciers in various regions. Moreover, while we only considered the semi-volatile species for the interactive pH calculation in this study (see Materials and Methods), an improved pH calculation in GEOS-Chem including contributions from dust alkalinity, sea salt aerosol alkalinity, and carboxylic acids shows consistency with annual mean precipitation pH observed at wide regions in NA, WE, and East Asia (58). Given the heterogeneous distribution of cloud pH (54, 58) and short lifetime (~4 to 5 days) of sulfate aerosols (46), improvements of the model constrained by spatio-temporal variations of Δ¹⁷O_{SO₄²⁻ are desirable in the future for model validation of sulfate formation pathways, sulfate burden, and prediction of aerosols-influencing climate change.}}}}}}

MATERIALS AND METHODS

Samples

This study is based on the 90.45-m-deep ice core obtained at a southeastern Greenland dome site (67.18°N, 36.37°W, 3170 m a.s.l.,

SE-Dome hereafter) (59). The age-depth scale was determined by the oxygen-isotope matching method with an estimated age error of 2 months (39). The ice core samples were stored in the cold room (-50°C) of The Institute of Low Temperature Science, Hokkaido University, Sapporo, Japan.

The ion fluxes of the species used in Fig. 1 are from a previous study (38). To match the resolution of ion fluxes and Δ¹⁷O_{SO₄²⁻, we reanalyzed the data with our resolutions as summarized in table S1. In addition to ion fluxes, we calculated the neutralization ratio (*N*) and H⁺ flux [*F*(H⁺)] determined by ion balance}

$$N = \text{NH}_4^+ / (2\text{nss-SO}_4^{2-} + \text{NO}_3^-) \quad (5)$$

$$F(\text{H}^+) = F(\text{Cl}^-) + 2F(\text{SO}_4^{2-}) + F(\text{NO}_3^-) - F(\text{Na}^+) - F(\text{K}^+) - 2F(\text{Mg}^{2+}) - 2F(\text{Ca}^{2+}) \quad (6)$$

where *F*(*X*) (nmol m³ year⁻¹) represents the flux of *X* as determined by Iizuka *et al.* (38), and nss refers to non-sea salt component.

Since sea salt sulfate aerosols (ss-SO₄²⁻) are of little importance to atmospheric sulfur oxidation processes (i.e., Δ¹⁷O_{ss-SO₄²⁻ = 0‰), Δ¹⁷O values were corrected for their sea salt sulfate (ss-SO₄²⁻) component to obtain their corresponding nss-SO₄²⁻ content, using Eq. 7 below.}

$$[\text{SO}_4^{2-}]_{\text{nss}} = [\text{SO}_4^{2-}]_{\text{total}} - \frac{[\text{SO}_4^{2-}]_{\text{seawater}}}{[\text{Na}^+]_{\text{seawater}}} \times [\text{Na}^+] \quad (7)$$

The molar ratio of [SO₄²⁻]_{seawater}/[Na⁺]_{seawater} in seawater is 0.06 (60).

Ice core cut

The ice sample was cut by a band saw in a cold room (-20°C) and decontaminated by cutting the outside ice with a ceramic knife to ~70% of the sample's original weight in a class 10,000 clean booth. The sample (approximately 1 to 2 kg) was then melted in a pre-cleaned bottle and shipped frozen (~-20°C) to the Tokyo Institute of Technology, Yokohama, Japan. The sample was then stored in a freezer kept at -30°C until the time of the experiments described below. The samples and corresponding years covered are summarized in table S1.

Oxygen isotope analysis of sulfate

Δ¹⁷O is the deviation from the linear approximation of δ¹⁷O = 0.52 × δ¹⁸O and defined as Δ¹⁷O = δ¹⁷O - 0.52 × δ¹⁸O (13), where δ^{17,18}O = [(^{17,18}O/¹⁶O)_{sample} / (^{17,18}O/¹⁶O)_{reference} - 1], and reference represents the composition of Vienna Standard Mean Ocean Water.

The measurement system for Δ¹⁷O_{SO₄²⁻} follows Savarino *et al.* (61), with modifications described in our previous study (25). SO₄²⁻ was separated from other ions using ion chromatography and converted to H₂SO₄. One micromole of H₂SO₄ was then chemically converted to Na₂SO₄, and 1 ml of 30% H₂O₂ solution was subsequently added and dried up. Next, the Na₂SO₄ was converted to silver sulfate (Ag₂SO₄) using an ion exchange resin (25). This Ag₂SO₄ powder was transported in a custom-made quartz cup, which was dropped into the 1000°C furnace of a high-temperature conversion elemental analyzer (TC/EA; Thermo Fisher Scientific, Bremen, Germany) and thermally decomposed into O₂ and SO₂. Gas products

from this sample pyrolysis were carried by ultrahigh-purity He (>99.99995% purity; Japan Air Gases Co., Tokyo, Japan), which was first purified using a molecular sieve (5 Å) held at -196°C (62). The O₂ and SO₂ gas products were carried through a clean-up trap (trap 1) held at -196°C to trap SO₂ and trace SO₃, while O₂ was transported to another tubing trap (1/16 inch outer diameter) with a molecular sieve (5 Å) (trap 2) held at -196°C to trap O₂ separately from the other gas products. The O₂ was purified using a gas chromatograph, with a CP-Molsieve (5 Å) column (0.32 mm inner diameter, 30 m length, and 10 μm film; Agilent Technologies Inc., Santa Clara, CA, USA) held at 40°C, before being introduced to the Isotope-ratio mass spectrometry (IRMS) system to measure *m/z* = 32, 33, and 34. As discussed by Schauer *et al.* (63), this method results in oxygen isotope exchange between the O₂ products and the quartz cups having Δ¹⁷O of 0‰ (64), as well as the quartz reactor, which shifts δ¹⁷O and δ¹⁸O, and thus Δ¹⁷O measurements. The shift in Δ¹⁷O_{SO₄²⁻ values was corrected by estimating the magnitude of the oxygen isotope exchange with quartz materials, whose Δ¹⁷O value is assumed to be approximately 0‰ (64). Note that the SO₄²⁻ δ¹⁷O and δ¹⁸O values here are relative values to our O₂ reference gas. The shift in Δ¹⁷O_{SO₄²⁻ due to exchange between quartz cup and samples was corrected by replicate analyses (*n* = 12) of the standard B (Δ¹⁷O_{SO₄²⁻ = 2.4‰) with three independent experimental batches of this study. The four standard B were measured in the run number of 1, 5, 8, and 10 for each batch. In this correction for isotopic analysis, SD (1σ) for the corrected values for standard B was 0.07‰, and this 1σ uncertainty is considered for the error of the isotopic measurement for this study.}}}

Equation 8 is the isotope mass balance equation between ss- and nss-SO₄²⁻ with Δ¹⁷O_{ss-SO₄²⁻ = 0‰}

$$\Delta^{17}\text{O}_{\text{nss-SO}_4^{2-}} = \frac{[\text{SO}_4^{2-}]_{\text{total}}}{[\text{SO}_4^{2-}]_{\text{nss}}} \times \Delta^{17}\text{O}_{\text{total-SO}_4^{2-}} \quad (8)$$

where “total” is the quantity measured by ion chromatography, corresponding to the sum of ss- and nss-SO₄²⁻ components. The data for Δ¹⁷O_{total-SO₄²⁻ and Δ¹⁷O_{nss-SO₄²⁻ are summarized in table S1. The overall observational error for Δ¹⁷O_{nss-SO₄²⁻ is calculated to be at or smaller than ±0.1‰ for ice core samples (table S1), based on propagation of the errors for ion concentrations of [Na⁺] and [SO₄²⁻]_{total} (±5%) and isotopic analysis (±0.07‰).}}}

GEOS-Chem model description and simulations

GEOS-Chem is a global three-dimensional model of atmospheric composition (www.geos-chem.org) originally developed by Bey *et al.* (65). In this study, we use GEOS-Chem (version 12.5.0, DOI: 10.5281/zenodo.3403111) driven by assimilated meteorological fields from MERRA-2 reanalysis data product from NASA Global Modeling and Assimilation Office’s GEOS-5 Data Assimilation System. We simulate aerosol-oxidant tropospheric chemistry containing detailed HO_x-NO_x-VOC-ozone-BrO_x chemistry (65–67). The model was run at 4° × 5° horizontal resolution and 47 vertical levels up to 0.01 hPa. The model was spun up for 1 year before each of the 5 years simulated. In the model, sulfate is produced from gas-phase oxidation of SO₂ (g) by OH, aqueous-phase oxidation of S(IV) by H₂O₂, O₃, HOBr, and O₂ catalyzed by TMI, and heterogeneous oxidation on sea salt aerosols by O₃ (36, 46).

The parameterization of the metal-catalyzed S(IV) oxidation is described in Alexander *et al.* (33). We consider Fe and Mn, which catalyze S(IV) oxidation, in the oxidation states of Fe(III) and

Mn(II). Dust-derived Fe ([Fe]_{dust}) is scaled to the modeled dust concentration as 3.5% of total dust mass, and dust-derived Mn is a factor of 50 times lower than [Fe]_{dust}. Anthropogenic Fe ([Fe]_{anthro}) is scaled as 1/30 of primary sulfate and anthropogenic Mn ([Mn]_{anthro}) is 10 times lower than that of [Fe]_{anthro}. In the model, 50% of Mn is dissolved in cloud water as Mn(II) oxidation state, and 1% of [Fe]_{dust} and 10% of [Fe]_{anthro} are dissolved in cloud water as Fe(III) oxidation states. This parameterization might underestimate the anthropogenic Fe and Mn, especially for the U.S. region, which is discussed in Supplementary Text.

For pH-dependent S(IV) partitioning, bulk cloud water pH is calculated iteratively using concentrations of sulfate, total nitrate (HNO₃ + NO₃⁻), total ammonia (NH₃ + NH₄⁺), SO₂, and CO₂ = 380 ppmv (parts per million by volume) based on their effective Henry’s law constants and the local cloud liquid water content as described in Alexander *et al.* (46). We use the Yuen *et al.* parameterization to account for the effect of heterogeneity of cloud water pH on S(IV) partitioning and subsequent aqueous phase sulfate formation (46). Sulfate formed from each oxidation pathway was treated as a different “tracer” in the model to calculate Δ¹⁷O as described elsewhere (32, 35).

Given that meteorological fields from MERRA-2 are not available before 1979, we use meteorological fields and nonanthropogenic emissions such as biogenic VOCs (42), soil NO_x (43), lightning (44), and stratospheric sources (44) from the year 1986, and set anthropogenic emissions, biomass burning emissions, and CH₄ concentrations to specific years. For anthropogenic emissions, we use the Community Emissions Data System (CEDS) inventory (<http://globalchange.umd.edu/ceds/>) (68). Emission species for CEDS include aerosol [black carbon (BC) and organic carbon (OC)], aerosol precursors, and reactive compounds [SO₂, NO_x, NH₃, CO, and non-methane volatile organic carbon (NMVOC)]. We use the biomass burning emissions from the CMIP6 (BB4CMIP) inventory for each individual year (69). Emission species for BB4CMIP include the following species: BC, CH₄, CO, NH₃, NMVOC, NO_x, OC, SO₂, and HCl. We prescribe latitudinal CH₄ concentrations for historical simulations. For years after 1979, CH₄ concentrations are based on the National Oceanic and Atmospheric Administration Earth System Research Laboratory (NOAA/ESRL) Global Monitoring Division flask observations (http://esrl.noaa.gov/gmd/ccgg/trends_ch4/), and for years before 1979, the CMIP6 monthly mean surface CH₄ is used (70).

The simulations were performed for years 1960, 1973, 1986, 1999, and 2013, which enables us to isolate the impact of anthropogenic emissions on historical changes in sulfate formation pathways and Δ¹⁷O_{SO₄²⁻ based on Eq. 1. We considered the error in the modeled Δ¹⁷O_{SO₄²⁻ by propagating the uncertainties of Δ¹⁷O_{SO₄²⁻(H₂O₂) and Δ¹⁷O_{SO₄²⁻(O₃), yielding 1σ uncertainty of smaller than 0.1‰ (table S3). In addition to the five model years with calculated cloud pH, we test the same model but assume cloud water pH is constant (pH 4.5) for 1973 and 2013, to examine the importance of changes in bulk cloud pH for modeled Δ¹⁷O_{SO₄²⁻ over the period.}}}}}

In addition to the calculation of the transported sulfate in the model, we also extracted online diagnostics to calculate sulfate production efficiency (η) using Eq. 4. S(SO₂) was calculated by summing the emission of SO₂ from anthropogenic and volcanic activity, photochemical production of SO₂ from dimethyl sulfide (DMS) oxidation in the atmosphere, and the net import/export budget of SO₂ by transportation. The production of SO₄²⁻ [P(SO₄²⁻)] was also calculated online as the sum from all aqueous, heterogeneous, and gas-phase production pathways.

SUPPLEMENTARY MATERIALS

Supplementary material for this article is available at <http://advances.sciencemag.org/cgi/content/full/7/19/eabd4610/DC1>

REFERENCES AND NOTES

- IPCC, *Climate Change 2013: The Physical Science Basis. Contribution of Working Group I to the Fifth Assessment Report of the Intergovernmental Panel on Climate Change* (Cambridge Univ. Press, 2013), 1535 pp.
- J. G. Watson, Visibility: Science and regulation. *J. Air Waste Manage. Assoc.* **52**, 628–713 (2002).
- A. J. Cohen, M. Brauer, R. Burnett, H. R. Anderson, J. Frostad, K. Estep, K. Balakrishnan, B. Brunekreef, L. Dandona, R. Dandona, V. Feigin, G. Freedman, B. Hubbell, A. Jobling, H. Kan, L. Knibbs, Y. Liu, R. Martin, L. Morawska, C. A. Pope III, H. Shin, K. Straif, G. Shaddick, M. Thomas, R. van Dingenen, A. van Donkelaar, T. Vos, C. J. L. Murray, M. H. Forouzanfar, Estimates and 25-year trends of the global burden of disease attributable to ambient air pollution: An analysis of data from the Global Burden of Diseases Study 2015. *Lancet* **389**, 1907–1918 (2017).
- P. T. Manktelow, G. W. Mann, K. S. Carslaw, D. V. Spracklen, M. P. Chipperfield, Regional and global trends in sulfate aerosol since the 1980s. *Geophys. Res. Lett.* **34**, (2007).
- J. L. Hand, B. A. Schichtel, W. C. Malm, M. L. Pitchford, Particulate sulfate ion concentration and SO₂ emission trends in the United States from the early 1990s through 2010. *Atmos. Chem. Phys.* **12**, 10353–10365 (2012).
- J. Feng, E. Chan, R. Vet, Air quality in the eastern United States and Eastern Canada for 1990–2015: 25 years of change in response to emission reductions of SO₂ and NO_x in the region. *Atmos. Chem. Phys.* **20**, 3107–3134 (2020).
- I. Faloon, Sulfur processing in the marine atmospheric boundary layer: A review and critical assessment of modeling uncertainties. *Atmos. Environ.* **43**, 2841–2854 (2009).
- J. H. Seinfeld, S. N. Pandis, *Atmospheric Chemistry and Physics: From Air Pollution to Climate Change* (John Wiley & Sons, 2012).
- V. Shah, L. Jaeglé, J. A. Thornton, F. D. Lopez-Hilfiker, B. H. Lee, J. C. Schroder, P. Campuzano-Jost, J. L. Jimenez, H. Guo, A. P. Sullivan, R. J. Weber, J. R. Green, M. N. Fiddler, S. Billig, T. L. Campos, M. Stell, A. J. Weinheimer, D. D. Montzka, S. S. Brown, Chemical feedbacks weaken the wintertime response of particulate sulfate and nitrate to emissions reductions over the eastern United States. *Proc. Natl. Acad. Sci. U.S.A.* **115**, 8110–8115 (2018).
- A. P. Tsipidi, V. A. Karydis, S. N. Pandis, Response of inorganic fine particulate matter to emission changes of sulfur dioxide and ammonia: The eastern United States as a case study. *J. Air Waste Manage. Assoc.* **57**, 1489–1498 (2007).
- F. Paulot, S. Fan, L. Horowitz, Contrasting seasonal responses of sulfate aerosols to declining SO₂ emissions in the Eastern U.S.: Implications for the efficacy of SO₂ emission controls. *Geophys. Res. Lett.* **44**, 455–464 (2017).
- J. Holt, N. E. Selin, S. Solomon, Changes in inorganic fine particulate matter sensitivities to precursors due to large-scale U.S. emissions reductions. *Environ. Sci. Technol.* **49**, 4834–4841 (2015).
- M. H. Thiemens, Mass-independent isotope effects in planetary atmospheres and the early solar system. *Science* **283**, 341–345 (1999).
- B. D. Holt, R. Kumar, P. T. Cunningham, Oxygen-18 study of the aqueous-phase oxidation of sulfur dioxide. *Atmos. Environ.* **15**, 557–566 (1981).
- J. Savarino, C. C. Lee, M. H. Thiemens, Laboratory oxygen isotopic study of sulfur (IV) oxidation: Origin of the mass-independent oxygen isotopic anomaly in atmospheric sulfates and sulfate mineral deposits on Earth. *J. Geophys. Res. Atmos.* **105**, 29079–29088 (2000).
- J. Savarino, M. H. Thiemens, Analytical procedure to determine both δ¹⁸O and δ¹⁷O of H₂O₂ in natural water and first measurements. *Atmos. Environ.* **33**, 3683–3690 (1999).
- D. Krankowsky, F. Bartecki, G. G. Klees, K. Mauersberger, K. Schellenbach, J. Stehr, Measurement of heavy isotope enrichment in tropospheric ozone. *Geophys. Res. Lett.* **22**, 1713–1716 (1995).
- J. C. Johnston, M. H. Thiemens, The isotopic composition of tropospheric ozone in three environments. *J. Geophys. Res. Atmos.* **102**, 25395–25404 (1997).
- J. Morton, J. Barnes, B. Schueler, K. Mauersberger, Laboratory studies of heavy ozone. *J. Geophys. Res. Atmos.* **95**, 901–907 (1990).
- M. H. Thiemens, T. Jackson, Pressure dependency for heavy isotope enhancement in ozone formation. *Geophys. Res. Lett.* **17**, 717–719 (1990).
- C. Janssen, J. Guenther, D. Krankowsky, K. Mauersberger, Temperature dependence of ozone rate coefficients and isotopologue fractionation in ¹⁶O–¹⁸O oxygen mixtures. *Chem. Phys. Lett.* **367**, 34–38 (2003).
- K. Mauersberger, D. Krankowsky, C. Janssen, in *Solar System History from Isotopic Signatures of Volatile Elements* (Springer, 2003), pp. 265–279.
- W. C. Vicars, J. Savarino, Quantitative constraints on the ¹⁷O-excess (Δ¹⁷O) signature of surface ozone: Ambient measurements from 50° N to 50° S using the nitrite-coated filter technique. *Geochim. Cosmochim. Acta* **135**, 270–287 (2014).
- J. Savarino, W. C. Vicars, M. Legrand, S. Preunkert, B. Jourdain, M. M. Frey, A. Kukui, N. Caillon, J. Gil Roca, Oxygen isotope mass balance of atmospheric nitrate at Dome C, East Antarctica, during the OPALE campaign. *Atmos. Chem. Phys.* **16**, 2659–2673 (2016).
- S. Ishino, S. Hattori, J. Savarino, B. Jourdain, S. Preunkert, M. Legrand, N. Caillon, A. Barbero, K. Kuribayashi, N. Yoshida, Seasonal variations of triple oxygen isotopic compositions of atmospheric sulfate, nitrate, and ozone at Dumont d'Urville, coastal Antarctica. *Atmospheric Chemistry and Physics* **17**, 3713–3727 (2017).
- J. R. Lyons, Transfer of mass-independent fractionation in ozone to other oxygen-containing radicals in the atmosphere. *Geophys. Res. Lett.* **28**, 3231–3234 (2001).
- C. C.-W. Lee, J. Savarino, M. H. Thiemens, Mass independent oxygen isotopic composition of atmospheric sulfate: Origin and implications for the present and past atmosphere of Earth and Mars. *Geophys. Res. Lett.* **28**, 1783–1786 (2001).
- P. He, B. Alexander, L. Geng, X. Chi, S. Fan, H. Zhan, H. Kang, G. Zheng, Y. Cheng, H. Su, C. Liu, Z. Xie, Isotopic constraints on heterogeneous sulfate production in Beijing haze. *Atmos. Chem. Phys.* **18**, 5515–5528 (2018).
- B. Alexander, J. Savarino, N. I. Barkov, R. J. Delmas, M. H. Thiemens, Climate driven changes in the oxidation pathways of atmospheric sulfur. *Geophys. Res. Lett.* **29**, 30-1–30-4 (2002).
- E. Gautier, J. Savarino, J. Hoek, J. Erbland, N. Caillon, S. Hattori, N. Yoshida, E. Albalat, F. Albaredo, J. Farquhar, 2600-years of stratospheric volcanism through sulfate isotopes. *Nat. Commun.* **10**, 466 (2019).
- B. Alexander, J. Savarino, K. J. Kreutz, M. H. Thiemens, Impact of preindustrial biomass-burning emissions on the oxidation pathways of tropospheric sulfur and nitrogen. *J. Geophys. Res. Atmos.* **109**, D08303 (2004).
- E. Sofen, B. Alexander, S. Kunasek, The impact of anthropogenic emissions on atmospheric sulfate production pathways, oxidants, and ice core Δ¹⁷O(SO₄²⁻). *Atmos. Chem. Phys.* **11**, 3565–3578 (2011).
- B. Alexander, R. J. Park, D. J. Jacob, S. Gong, Transition metal catalyzed oxidation of atmospheric sulfur: Global implications for the sulfur budget. *J. Geophys. Res.* **114**, D02309 (2009).
- B. Alexander, R. J. Park, Q. B. Li, R. M. Yantosca, J. Savarino, C. C. W. Lee, M. H. Thiemens, Sulfate formation in sea-salt aerosols: Constraints on oxygen isotopes. *J. Geophys. Res. Atmos.* **110**, D10307 (2005).
- Q. Chen, L. Geng, J. A. Schmidt, Z. Xie, H. Kang, J. Dachs, J. Cole-Dai, A. J. Schauer, M. G. Camp, B. Alexander, Isotopic constraints on the role of hypohalous acids in sulfate aerosol formation in the remote marine boundary layer. *Atmos. Chem. Phys.* **16**, 11433–11450 (2016).
- Q. Chen, J. A. Schmidt, V. Shah, L. Jaeglé, T. Sherwen, B. Alexander, Sulfate production by reactive bromine: Implications for the global sulfur and reactive bromine budgets. *Geophys. Res. Lett.* **44**, 7069–7078 (2017).
- J. Shao, Q. Chen, Y. Wang, X. Lu, P. He, Y. Sun, V. Shah, R. V. Martin, S. Philip, S. Song, Y. Zhao, Z. Xie, L. Zhang, B. Alexander, Heterogeneous sulfate aerosol formation mechanisms during wintertime Chinese haze events: Air quality model assessment using observations of sulfate oxygen isotopes in Beijing. *Atmos. Chem. Phys.* **19**, 6107–6123 (2019).
- Y. Iizuka, R. Uemura, K. Fujita, O. Seki, C. Miyamoto, T. Suzuki, N. Yoshida, H. Motoyama, S. Motoba, A 60 year record of atmospheric aerosol depositions preserved in a high-accumulation dome ice core, Southeast Greenland. *J. Geophys. Res. Atmos.* **123**, 574–589 (2018).
- R. Furukawa, R. Uemura, K. Fujita, J. Sjolte, K. Yoshimura, S. Matoba, Y. Iizuka, Seasonal-scale dating of a shallow ice core from Greenland using oxygen isotope matching between data and simulation. *J. Geophys. Res. Atmos.* **122**, 10,873–10,887 (2017).
- Ø. A. Garmo, B. L. Skjelkvåle, H. A. de Wit, L. Colombo, C. Curtis, J. Fölster, A. Hoffmann, J. Hruška, T. Högåsen, D. S. Jeffries, W. B. Keller, P. Krám, V. Majer, D. T. Monteith, A. M. Paterson, M. Rogora, D. Rzychon, S. Steingruber, J. L. Stoddard, J. Vuorenmaa, A. Worsztynowicz, Trends in surface water chemistry in acidified areas in Europe and North America from 1990 to 2008. *Water Air Soil Pollut.* **215**, 1880 (2014).
- H. A. Kjaer, P. Vallelonga, A. Svensson, M. E. L. Kristensen, C. Tibuleac, M. Winstrup, S. Kipfstuhl, An optical dye method for continuous determination of acidity in ice cores. *Environ. Sci. Technol.* **50**, 10485–10493 (2016).
- M. Crippa, D. Guizzardi, M. Muntean, E. Schaaf, F. Dentener, J. A. van Aardenne, S. Monni, U. Doering, J. G. J. Olivier, G. Janssens-Maenhout, Gridded emissions of air pollutants for the period 1970–2012 within EDGAR v4.3.2. *Earth Syst. Sci. Data* **10**, 1987–2013 (2018).
- O. R. Cooper, D. D. Parrish, J. Ziemke, N. V. Balashov, M. Cupeiro, I. E. Galbally, S. Gilge, L. Horowitz, N. R. Jensen, J.-F. Lamarque, V. Naik, S. J. Oltmans, J. Schwab, D. T. Shindell, A. M. Thompson, V. Thouret, Y. Wang, R. M. Zbinden, Global distribution and trends of tropospheric ozone: An observation-based review. *Elementa* **2**, 000029 (2014).
- M. Rigby, S. A. Montzka, R. G. Prinn, J. W. C. White, D. Young, S. O'Doherty, M. F. Lunt, A. L. Ganesan, A. J. Manning, P. G. Simmonds, P. K. Salameh, C. M. Harth, J. Mühle, R. F. Weiss, P. J. Fraser, L. P. Steele, P. B. Krummel, A. McCulloch, S. Park, Role of atmospheric oxidation in recent methane growth. *Proc. Natl. Acad. Sci. U.S.A.* **114**, 5373–5377 (2017).

45. A. Sigg, A. Neftel, Evidence for a 50% increase in H₂O₂ over the past 200 years from a Greenland ice core. *Nature* **351**, 557–559 (1991).
46. B. Alexander, D. J. Allman, H. M. Amos, T. D. Fairlie, J. Dachs, D. A. Hegg, R. S. Sletten, Isotopic constraints on sulfate aerosol formation pathways in the marine boundary layer of the subtropical northeast Atlantic Ocean. *J. Geophys. Res.* **117**, D06304 (2012).
47. F. Paulot, D. J. Jacob, R. W. Pinder, J. O. Bash, K. Travis, D. K. Henze, Ammonia emissions in the United States, European Union, and China derived by high-resolution inversion of ammonium wet deposition data: Interpretation with a new agricultural emissions inventory (MASAGE_NH3). *J. Geophys. Res. Atmos.* **119**, 4343–4364 (2014).
48. K. E. Lamb, M. D. Dolan, D. F. Kennedy, Ammonia for hydrogen storage: A review of catalytic ammonia decomposition and hydrogen separation and purification. *Int. J. Hydrogen Energy* **44**, 3580–3593 (2019).
49. C. Li, C. McLinden, V. Fioletov, N. Krotkov, S. Carn, J. Joiner, D. Streets, H. He, X. Ren, Z. Li, R. Dickerson, India is overtaking China as the world's largest emitter of anthropogenic sulfur dioxide. *Sci. Rep.* **7**, 14304 (2017).
50. Y. Si, C. Yu, L. Zhang, W. Zhu, K. Cai, L. Cheng, L. Chen, S. Li, Assessment of satellite-estimated near-surface sulfate and nitrate concentrations and their precursor emissions over China from 2006 to 2014. *Sci. Total Environ.* **669**, 362–376 (2019).
51. G. J. Roelofs, P. Stier, J. Feichter, E. Vignati, J. Wilson, Aerosol activation and cloud processing in the global aerosol-climate model ECHAM5-HAM. *Atmos. Chem. Phys.* **6**, 2389–2399 (2006).
52. S. T. Turnock, G. W. Mann, M. T. Woodhouse, M. Dalvi, F. M. O'Connor, K. S. Carslaw, D. V. Spracklen, The impact of changes in cloud water pH on aerosol radiative forcing. *Geophys. Res. Lett.* **46**, 4039–4048 (2019).
53. T. Takemura, Return to different climate states by reducing sulphate aerosols under future CO₂ concentrations. *Sci. Rep.* **10**, 21748 (2020).
54. H. O. T. Pye, A. Nenes, B. Alexander, A. P. Ault, M. C. Barth, S. L. Clegg, J. L. Collett Jr., K. M. Fahey, C. J. Hennigan, H. Herrmann, M. Kanakidou, J. T. Kelly, I. T. Ku, V. F. McNeill, N. Riemer, T. Schaefer, G. Shi, A. Tilgner, J. T. Walker, T. Wang, R. Weber, J. Xing, R. A. Zaveri, A. Zuend, The acidity of atmospheric particles and clouds. *Atmos. Chem. Phys.* **20**, 4809–4888 (2020).
55. M. Chin, D. J. Jacob, G. M. Gardner, M. S. Foreman-Fowler, P. A. Spiro, D. L. Savoie, A global three-dimensional model of tropospheric sulfate. *J. Geophys. Res. Atmos.* **101**, 18667–18690 (1996).
56. D. Koch, D. Jacob, I. Tegen, D. Rind, M. Chin, Tropospheric sulfur simulation and sulfate direct radiative forcing in the Goddard Institute for Space Studies general circulation model. *J. Geophys. Res. Atmos.* **104**, 23799–23822 (1999).
57. S. Banzhaf, M. Schaap, A. Kerschbaumer, E. Reimer, R. Stern, E. van der Swaluw, P. Bultjes, Implementation and evaluation of pH-dependent cloud chemistry and wet deposition in the chemical transport model REM-Calgrid. *Atmos. Environ.* **49**, 378–390 (2012).
58. V. Shah, D. J. Jacob, J. M. Moch, X. Wang, S. Zhai, Global modeling of cloud water acidity, precipitation acidity, and acid inputs to ecosystems. *Atmos. Chem. Phys.* **20**, 12223–12245 (2020).
59. Y. Iizuka, S. Motaba, T. Yamasaki, I. Oyabu, M. Kadota, T. Aoki, Glaciological and meteorological observations at the SE-Dome site, southeastern Greenland Ice Sheet. *Bull. Glaciol. Res.* **34**, 1–10 (2016).
60. H. D. Holland, B. Lazar, M. McCaffrey, Evolution of the atmosphere and oceans. *Nature* **320**, 27–33 (1986).
61. J. Savarino, B. Alexander, V. Darmohusodo, M. H. Thiemens, Sulfur and oxygen isotope analysis of sulfate at micromole levels using a pyrolysis technique in a continuous flow system. *Anal. Chem.* **73**, 4457–4462 (2001).
62. S. Hattori, A. Toyoda, S. Toyoda, S. Ishino, Y. Ueno, N. Yoshida, Determination of the sulfur isotope ratio in carbonyl sulfide using gas chromatography/isotope ratio mass spectrometry on fragment ions ³²S⁺, ³³S⁺, and ³⁴S⁺. *Anal. Chem.* **87**, 477–484 (2015).
63. A. J. Schauer, S. A. Kunasek, E. D. Sofen, J. Erbland, J. Savarino, B. W. Johnson, H. M. Amos, R. Shaheen, M. Abaunza, T. L. Jackson, M. H. Thiemens, B. Alexander, Oxygen isotope exchange with quartz during pyrolysis of silver sulfate and silver nitrate. *Rapid Commun. Mass Spectrom.* **26**, 2151–2157 (2012).
64. Y. Matsuhisa, J. R. Goldsmith, R. N. Clayton, Mechanisms of hydrothermal crystallization of quartz at 250 C and 15 kbar. *Geochim. Cosmochim. Acta* **42**, 173–182 (1978).
65. I. Bey, D. J. Jacob, R. M. Yantosca, J. A. Logan, B. D. Field, A. M. Fiore, Q. Li, H. Y. Liu, L. J. Mickley, M. G. Schultz, Global modeling of tropospheric chemistry with assimilated meteorology: Model description and evaluation. *J. Geophys. Res. Atmos.* **106**, 23073–23095 (2001).
66. H. O. T. Pye, H. Liao, S. Wu, L. J. Mickley, D. J. Jacob, D. K. Henze, J. H. Seinfeld, Effect of changes in climate and emissions on future sulfate-nitrate-ammonium aerosol levels in the United States. *J. Geophys. Res. Atmos.* **114**, (2009).
67. T. Sherwen, J. A. Schmidt, M. J. Evans, L. J. Carpenter, K. Großmann, S. D. Eastham, D. J. Jacob, B. Dix, T. K. Koenig, R. Sinreich, I. Ortega, R. Volkamer, A. Saiz-Lopez, C. Prados-Roman, A. S. Mahajan, C. Ordóñez, Global impacts of tropospheric halogens (Cl, Br, I) on oxidants and composition in GEOS-Chem. *Atmos. Chem. Phys.* **16**, 12239–12271 (2016).
68. R. M. Hoesly, S. J. Smith, L. Feng, Z. Klimont, G. Janssens-Maenhout, T. Pitkanen, J. J. Seibert, L. Vu, R. J. Andres, R. M. Bolt, T. C. Bond, L. Dawidowski, N. Khodol, J. I. Kurokawa, M. Li, L. Liu, Z. Lu, M. C. P. Moura, P. R. O'Rourke, Q. Zhang, Historical (1750–2014) anthropogenic emissions of reactive gases and aerosols from the Community Emissions Data System (CEDS). *Geosci. Model Dev.* **11**, 369–408 (2018).
69. M. J. E. van Marle, S. Kloster, B. I. Magi, J. R. Marlon, A. L. Daniau, R. D. Field, A. Arneth, M. Forrester, S. Hantson, N. M. Kehrwald, W. Knorr, G. Lasslop, F. Li, S. Mangeon, C. Yue, J. W. Kaiser, G. R. van der Werf, Historic global biomass burning emissions for CMIP6 (BB4CMIP) based on merging satellite observations with proxies and fire models (1750–2015). *Geosci. Model Dev.* **10**, 3329–3357 (2017).
70. M. Meinshausen, E. Vogel, A. Nauels, K. Lorbacher, N. Meinshausen, D. M. Etheridge, P. J. Fraser, S. A. Montzka, P. J. Rayner, C. M. Trudinger, P. B. Krummel, U. Beyerle, J. G. Canadell, J. S. Daniel, I. G. Enting, R. M. Law, C. R. Lunder, S. O'Doherty, R. G. Prinn, S. Reimann, M. Rubino, G. J. M. Velders, M. K. Vollmer, R. H. J. Wang, R. Weiss, Historical greenhouse gas concentrations for climate modelling (CMIP6). *Geosci. Model Dev.* **10**, 2057–2116 (2017).
71. W. C. Vicars, S. K. Bhattacharya, J. Erbland, J. Savarino, Measurement of the ¹⁷O-excess (Δ¹⁷O) of tropospheric ozone using a nitrite-coated filter. *Rapid Commun. Mass Spectrom.* **26**, 1219–1231 (2012).
72. Q. Liu, L. M. Schurter, C. E. Muller, S. Aloisio, J. S. Francisco, D. W. Margerum, Kinetics and mechanisms of aqueous ozone reactions with bromide, sulfite, hydrogen sulfite, iodide, and nitrite ions. *Inorg. Chem.* **40**, 4436–4442 (2001).
73. A. Reff, P. V. Bhavne, H. Simon, T. G. Pace, G. A. Pouliot, J. D. Mobley, M. Houyoux, Emissions inventory of PM_{2.5} trace elements across the United States. *Environ. Sci. Technol.* **43**, 5790–5796 (2009).
74. P.-F. Yuen, D. A. Hegg, T. V. Larson, M. C. Barth, Parameterization of heterogeneous droplet chemistry for use in bulk cloud models. *J. Appl. Meteorol.* **35**, 679–689 (1996).

Acknowledgments: We gratefully acknowledge the drilling and initial analysis teams of SE-Dome. We thank P. Akers for editing a draft of this manuscript. **Funding:** This work was supported by MEXT/JSPS KAKENHI grant nos. JP16H05884, JP18H05292, JP17H06105, JP18H03363, and JP20H04305. This study was part of the Joint Research and the Leadership programs of the Institute of Low Temperature Science, Hokkaido University, and ArCS II (Arctic Challenge for Sustainability II), Program grant no. JPMXD1420318865). S.H. appreciates support for this project from JSPS and CNRS under the JSPS-CNRS Joint Research Program. B.A. acknowledges support from NSF AGS 1702266 and NSF PLR 1904128. We are grateful to the Global Modeling and Assimilation Office (GMAO) at NASA Goddard Space Flight Center for providing the MERRA-2 meteorological data used to drive the modeling in this study. **Author contributions:** S.H. designed the research. Y.I. and S.M. performed the field work and sampling. S.H., Y.I., S.I., N.S., A.T., and N.Y. contributed to the isotopic measurements. S.H., Y.I., R.U., K.F., N.O., and J.S. analyzed the data. S.H., B.A., S.I., S.Z., T.S., and A.Y. contributed to the model simulations. S.H. wrote the paper with contributions from all co-authors. **Competing interests:** The authors declare that they have no competing interests. **Data and materials availability:** All data needed to evaluate the conclusions in the paper are present in the paper and/or the Supplementary Materials. Additional data related to this paper may be requested from the authors.

Submitted 22 June 2020
Accepted 16 March 2021
Published 5 May 2021
10.1126/sciadv.abd4610

Citation: S. Hattori, Y. Iizuka, B. Alexander, S. Ishino, K. Fujita, S. Zhai, T. Sherwen, N. Oshima, R. Uemura, A. Yamada, N. Suzuki, S. Matoba, A. Tsuruta, J. Savarino, N. Yoshida, Isotopic evidence for acidity-driven enhancement of sulfate formation after SO₂ emission control. *Sci. Adv.* **7**, eabd4610 (2021).

Isotopic evidence for acidity-driven enhancement of sulfate formation after SO₂ emission control

Shohei Hattori, Yoshinori Iizuka, Becky Alexander, Sakiko Ishino, Koji Fujita, Shuting Zhai, Tomás Sherwen, Naga Oshima, Ryu Uemura, Akinori Yamada, Nozomi Suzuki, Sumito Matoba, Asuka Tsuruta, Joel Savarino and Naohiro Yoshida

Sci Adv 7 (19), eabd4610.
DOI: 10.1126/sciadv.abd4610

ARTICLE TOOLS

<http://advances.sciencemag.org/content/7/19/eabd4610>

SUPPLEMENTARY MATERIALS

<http://advances.sciencemag.org/content/suppl/2021/05/03/7.19.eabd4610.DC1>

REFERENCES

This article cites 69 articles, 3 of which you can access for free
<http://advances.sciencemag.org/content/7/19/eabd4610#BIBL>

PERMISSIONS

<http://www.sciencemag.org/help/reprints-and-permissions>

Use of this article is subject to the [Terms of Service](#)

Science Advances (ISSN 2375-2548) is published by the American Association for the Advancement of Science, 1200 New York Avenue NW, Washington, DC 20005. The title *Science Advances* is a registered trademark of AAAS.

Copyright © 2021 The Authors, some rights reserved; exclusive licensee American Association for the Advancement of Science. No claim to original U.S. Government Works. Distributed under a Creative Commons Attribution NonCommercial License 4.0 (CC BY-NC).